Quantum spin state transitions in the spin-1 equilateral triangular lattice antiferromagnet $Na_2BaNi(PO_4)_2$

N. Li,[1,*] Q. Huang,[2,*] A. Brassington,[2] X. Y. Yue,[3] W. J. Chu,[1] S. K. Guang,[1] X. H. Zhou,[1] P. Gao,[1] E. X. Feng,[4] H. B. Cao,[4] E. S. Choi,[5] Y. Sun,[3] Q. J. Li,[6] X. Zhao,[7] H. D. Zhou,[2,†] and X. F. Sun[1,3,8,‡]

[1]*Department of Physics, Hefei National Laboratory for Physical Sciences at Microscale, and Key Laboratory of Strongly-Coupled Quantum Matter Physics (CAS), University of Science and Technology of China, Hefei, Anhui 230026, People's Republic of China*

[2]*Department of Physics and Astronomy, University of Tennessee, Knoxville, Tennessee 37996-1200, USA*

[3]*Institute of Physical Science and Information Technology, Anhui University, Hefei, Anhui 230601, People's Republic of China*

[4]*Neutron Scattering Division, Oak Ridge National Laboratory, Oak Ridge, Tennessee 37831, USA*

[5]*National High Magnetic Field Laboratory, Florida State University, Tallahassee, Florida 32310-3706, USA*

[6]*School of Physics and Material Sciences, Anhui University, Hefei, Anhui 230601, People's Republic of China*

[7]*School of Physical Sciences, University of Science and Technology of China, Hefei, Anhui 230026, People's Republic of China*

[8]*Collaborative Innovation Center of Advanced Microstructures, Nanjing University, Nanjing, Jiangsu 210093, People's Republic of China*

(Received 28 June 2021; accepted 23 August 2021; published 1 September 2021)

We have grown single crystals of $Na_2BaNi(PO_4)_2$, a spin-1 equilateral triangular lattice antiferromagnet (ETLAF), and performed magnetic susceptibility, specific heat, and thermal conductivity measurements at ultralow temperatures. The main results are as follows: (i) At zero magnetic field, $Na_2BaNi(PO_4)_2$ exhibits a magnetic ordering at 430 mK with a weak ferromagnetic moment along the c axis. This suggests a canted 120° spin structure, which is in a plane including the crystallographic c axis due to the existence of an easy-axis anisotropy and ferromagnetically stacked along the c axis. (ii) With increasing field along the c axis, a 1/3 magnetization plateau is observed, which means that the canted 120° spin structure is transformed into an up-up-down (UUD) spin structure. With even higher fields, the UUD phase further evolves into possible V and V′ phases. (iii) With increasing field along the a axis, the canted 120° spin structure is possibly transformed into an umbrella phase and a V phase. Therefore $Na_2BaNi(PO_4)_2$ is a rare example of a spin-1 ETLAF with single-crystalline form that exhibits easy-axis spin anisotropy and a series of quantum spin state transitions.

DOI: 10.1103/PhysRevB.104.104403

I. INTRODUCTION

The two-dimensional (2D) equilateral triangular lattice antiferromagnet (ETLAF) with spin-1/2 is one of the simplest geometrically frustrated systems with strong quantum spin fluctuations, which recently has caught attention due to its exotic quantum magnetism. One celebrated example is the quantum spin liquid (QSL) [1–4] that can host non-Abelian quasiparticle [5] and fractional excitations [6,7] known as spinons [8,9], which allows quantum mechanical encryption and transportation of information with potential for creating a qubit that is protected against environmental influences [10]. For example, the recently studied $NaYbO_2$ [11], $NaYbS_2$ [12–14], $NaYbSe_2$ [15–17], $CsYbSe_2$ [18,19], and $YbMgGaO_4$ [20–28] are ETLAFs with effective spin-1/2 for Yb^{3+} ions and have been proposed as QSL candidates. Due to the Mg/Ga site disorder, the ground state of $YbMgGaO_4$ [29–34] also has been proposed as a spin-glass or random spin singlet state.

Another example of exotic magnetism in spin-1/2 ETLAFs is the quantum spin state transition (QSST). Theoretical studies have proposed that in a spin-1/2 ETLAF, the quantum spin fluctuations stabilize a novel up-up-down (UUD) phase while approaching zero temperature with the applied field parallel to either the easy plane or the easy axis [35,36]. This UUD phase exhibits itself as a magnetization plateau within a certain magnetic field regime and with one-third of the saturation magnetization (1/3 M_s). Experimentally, such a UUD phase has been reported for $Ba_3CoSb_2O_9$ [37–40], $Ba_3CoNb_2O_9$ [41,42], $Ba_2La_2CoTe_2O_{12}$ [43], and $Na_2BaCo(PO_4)_2$ [44], all of which are ETLAFs with effective spin-1/2 for Co^{2+} ions. In some cases the QSL and QSST are correlated. It has been reported that the QSL state can be tuned to the UUD phase by an applied magnetic field in these Yb-ETLAFs mentioned above [11,12,15,18]. Meanwhile, for $Na_2BaCo(PO_4)_2$, although it orders at $T_N = 148$ mK, the observed residual term of thermal conductivity (κ_0/T) suggests that it behaves as a QSL with itinerant excitations above its T_N [44].

To better understand the quantum magnetism of spin-1/2 ETLAFs, a useful approach is to switch the spin number. For example, one can replace the spin 1/2 by spin 1 and study how the quantum magnetism of the ETLAFs changes accordingly. The reported studies on spin-1 ETLAFs are limited. So far, the UUD phase has been reported for the 6HA phase

*These authors contributed equally to this work.
†hzhou10@utk.edu
‡xfsun@ustc.edu.cn

of $Ba_3NiSb_2O_9$ [45], $Ba_3NiNb_2O_9$ [46], $Ba_2La_2NiTe_2O_{12}$ [47], and the QSL has been proposed for 6HB phase of $Ba_3NiSb_2O_9$ [48–51], all of which are spin-1 ETLAFs for Ni^{2+} ions.

In this paper, we synthesized the spin-1 ETLAF $Na_2BaNi(PO_4)_2$ and grew single-crystal samples to perform dc and ac magnetic susceptibility, specific heat, and thermal conductivity measurements. The results show that it orders at $T_N = 430$ mK with a weak ferromagnetic moment and exhibits a $1/3$ M_s plateau (the UUD phase) with magnetic field applied along the c axis, both of which suggest an easy-axis anisotropy. The obtained magnetic phase diagrams show more field-induced spin state transitions besides the UUD phase.

II. EXPERIMENTS

The polycrystalline samples of $Na_2BaNi(PO_4)_2$ was firstly made by solid-state reaction. The stoichiometric mixtures of $NaCO_3$, $BaCO_3$, $NiCO_3$, and $(NH_4)_2HPO_4$ were ground together and then annealed in air at 300, 600 and 700 °C for 20 h successively. The single-crystal sample was prepared by following the reported procedure used for single-crystal growth of $Na_2BaCo(PO_4)_2$ [52]. The polycrystalline sample $Na_2BaNi(PO_4)_2$ and NaCl were mixed inside a Pt crucible with the mass ratio 1:5. The mixture was heated up to 950 °C for 2 h and then cooled down to 750 °C with a rate of 3 °C/h. The obtained crystals are thin plates with yellow color. The single-crystal x-ray diffraction data were collected at 250 K with the Mo K_α radiation (0.710 73 Å) using a Rigaku Xtalab Pro diffractometer at Oak Ridge National Laboratory's neutron scattering user facility. The data reduction was done with CRYSALISPRO, and the refinement was done with FULLPROF [53].

The dc magnetic susceptibility χ was measured with a Quantum Design superconducting quantum interference device (SQUID) magnetometer with a zero-field-cooling process and a dc magnetic field $B = 0.1$ T. The dc magnetization with a magnetic field up to 14 T was measured using a physical property measurement system (PPMS, Quantum Design). The ac susceptibility (χ') measurements were conducted with a voltage-controlled current source (Stanford Research, No. CS580) and lock-in amplifier (Stanford Research, No. SR830) [54]. The phase of the lock-in amplifier is set to measure the first harmonic signal. The rms amplitude of the ac excitation field is set to be 0.6 Oe with the frequency fixed at 220 Hz. The measurements were performed at SCM1 of the National High Magnetic Field Laboratory, Tallahassee, by using a dilution refrigerator. The data were obtained by the zero-field-cooling process, and we increased the magnetic field during the ramping process.

Specific heat C_p measurement was performed by using the relaxation method on a PPMS (Quantum Design) equipped with a dilution refrigerator insert. Thermal conductivity κ was measured using a "one heater, two thermometers" technique in a ^{3}He refrigerator at 300 mK $< T <$ 30 K and a ^{3}He / ^{4}He dilution refrigerator at 70 mK $< T <$ 1 K, equipped with a 14-T magnet [44,55,56]. The sample was cut precisely along the crystallographic axes with dimensions of $2.67 \times 0.73 \times 0.14$ mm^3, where the longest and the shortest dimensions are along the a and c axis, respectively. The heat current was applied along the a axis, while the magnetic field was applied along either the a or c axis.

III. RESULTS

A. Crystal structure

The as-grown crystals of $Na_2BaNi(PO_4)_2$ are thin plates with several-millimeter size, as shown in Fig. 1(a). The plate is normal to the crystallographic c axis, as confirmed by the Laue back-diffraction pattern [Fig. 1(b)]. The best refinement of the single-crystal diffraction data [Fig. 1(c)] leads to a $P\bar{3}$ space group. The detailed crystallographic parameters and atomic positions are listed in Tables I and II, respectively. The crystal structure is shown in Fig. 1(d), in which the triangular layers of magnetic NiO_6 octahedra are separated by a single layer of nonmagnetic BaO_{12} polyhedra, with $[PO_4]^{3-}$ units and Na^+ filling the gaps in the nickel oxide layers. This structure is very similar to that of $Na_2BaCo(PO_4)_2$ with the $P\bar{3}m1$ space group but with some differences. Compared with the $P\bar{3}m1$ space group [shown in Fig. 1(e)], in the $P\bar{3}$ space group [Fig. 1(f)] the nonmagnetic BaO_{12} polyhedra are fixed but the NiO_6 octahedra and PO_4 tetrahedra rotate in the opposite direction along the c axis [Fig. 1(f)]. Therefore the mirror plane symmetry in $Na_2BaCo(PO_4)_2$ is eliminated in $Na_2BaNi(PO_4)_2$.

B. dc and ac susceptibility

Figures 2(a) and 2(b) show the temperature dependence of the inverse dc susceptibility, $1/\chi$, for $B \parallel c$ and $B \parallel a$, respectively. The data show no sign of magnetic ordering down to 2 K and can be well fitted by the Curie-Weiss law with $\mu_{\text{eff}} = 3.56(1)$ μ_B and $\theta_{CW} = -1.2(1)$ K for $B \parallel c$ and with $\mu_{\text{eff}} = 3.26(1)$ μ_B, and $\theta_{CW} = -1.9(1)$ K for $B \parallel a$. Figures 2(c) and 2(d) show the dc magnetization measured at 2 K for $B \parallel c$ and $B \parallel a$, respectively. The saturation moments are 2.14(5) μ_B for $B \parallel c$ and 2.00(5) μ_B for $B \parallel a$. The g factors parallel and perpendicular to the c axis were evaluated to be $g_\parallel = 2.14(5)$ and $g_\perp = 2.00(5)$.

Figure 3(a) shows the temperature dependence of the ac susceptibility, $\chi'(T)$, measured at zero dc magnetic field ($B = 0$ T) but with the ac excitation field along the c axis. The curve shows a rapid increase below ~400 mK (defined as the Néel temperature T_N), indicating a magnetic ordering, similar to that observed in some other ETLAFs such as $Ba_2La_2NiTe_2O_{12}$ [47]. For the data measured with the ac excitation field along the a axis [Fig. 3(b)], this feature is not so clear. With an applied magnetic field along both the c and a axes, $\chi'(T)$ shows a peak at T_N [Figs. 3(c) and 3(d)]. With increasing field, this peak first shifts to higher temperatures while $B \leqslant 1$ T and then comes back to lower temperatures while $1 < B \leqslant 2.5$ T. For the data measured with $B \parallel a$ and $B = 0.5$ and 1.0 T, another additional peak is observed below T_N, which is labeled as T^* in Fig. 3(d).

Figure 4(a) shows the field dependence of $\chi'(B)$ measured at different temperatures with $B \parallel c$. At 20 mK, with increasing field, $\chi'(B)$ first quickly drops to a flat regime at $B_{c1} = 0.32(2)$ T, then exhibits two peaks at $B_{c2} = 1.72(1)$ T and $B_{c3} = 1.80(1)$ T, and finally drops to be flat again at $B_{c4} = 2.84(2)$ T. With increasing temperature, B_{c1} and B_{c2}

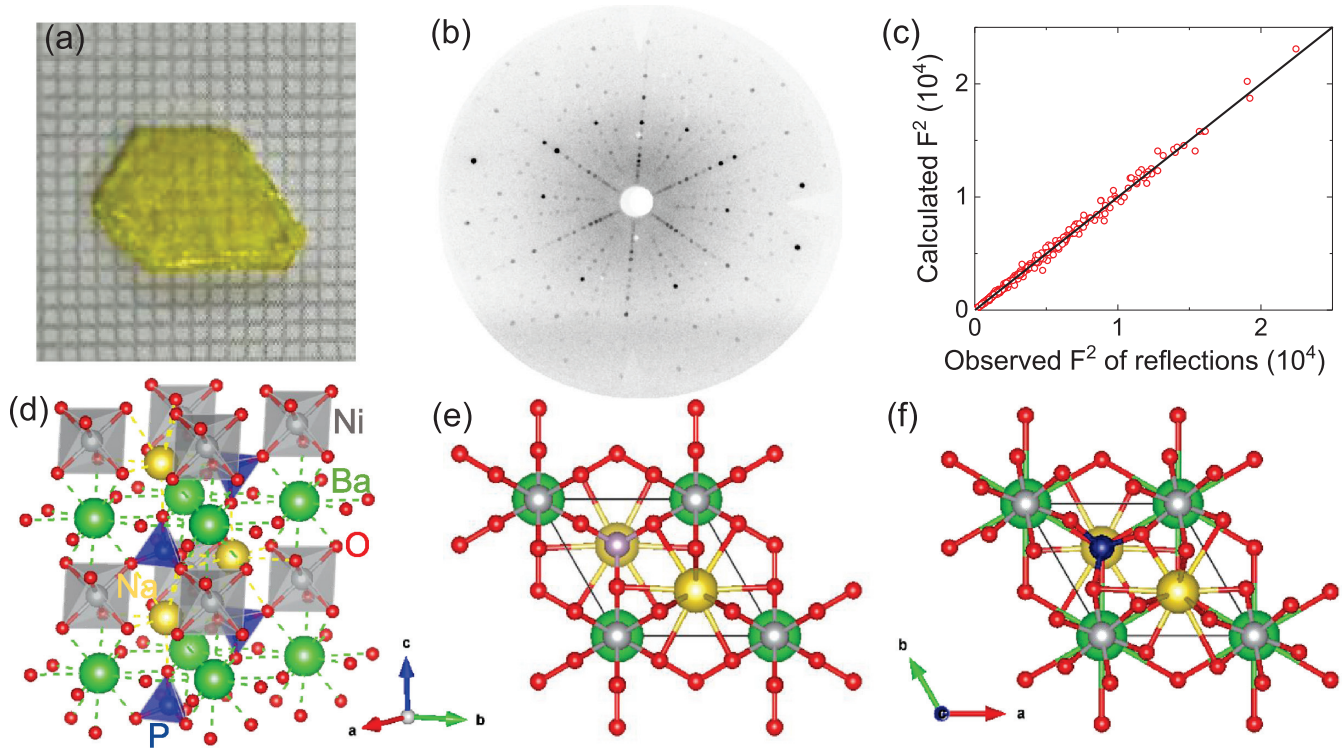

FIG. 1. (a) As-grown single crystal of $Na_2BaNi(PO_4)_2$. The scale of the grid is 1 mm. (b) Laue back-diffraction pattern along the crystallographic c axis. (c) Comparison between the observed squared structure factors at 250 K by single-crystal x-ray diffraction and the calculated ones based on the $P\bar{3}$ structure. (d) Illustration of the crystal structure for $Na_2BaNi(PO_4)_2$. (e) and (f) Projection of the crystal structure along the c axis for $Na_2BaCo(PO_4)_2$ with $P\bar{3}m1$ (e) and for $Na_2BaNi(PO_4)_2$ with $P\bar{3}$ (f)

shift to higher and lower fields, respectively, while B_{c3} and B_{c4} show no obvious change. Meanwhile, the peaks around B_{c2} and B_{c3} become broader with increasing temperature and disappear with temperature above 410 mK. Since the measured $\chi'(B)$ shows no frequency dependence (not shown here), it could be approximately treated as the derivative of the dc magnetization $M(B)$. Thus we calculated $M(B)$ by integrating $\chi'(B)$. The obtained $M(B)$ at 20 mK [Fig. 4(c)] clearly shows a plateau regime between B_{c1} and B_{c2} and a slope change at B_{c3} followed by the saturation around B_{c4}. Although we cannot infer the absolute value of $M(B)$ here, it is obvious that the magnetization of the plateau (around 0.32; here, we scaled the M value to the 5.0 T value) is around 1/3 of the saturation value (1.0).

Figure 4(b) shows $\chi'(B)$ with $B \parallel a$. At 20 mK, the curve shows two peaks at $B_{a1} = 0.230(2)$ T and $B_{a2} = 2.80(2)$ T, respectively, and then drops to be flat at $B_{a3} = 4.00(5)$ T. With increasing temperature, both peaks become broader and the B_{a1} peak shifts to higher fields while the B_{a2} peak shifts to lower fields. Above 300 mK, the peaks disappear. The calculated $M(B)$ at 20 mK with $B \parallel a$ [Fig. 4(d)] shows no obvious sign of the magnetization plateau, which is clearly different from that for $B \parallel c$.

TABLE I. Data of crystallographic refinement for $Na_2BaNi(PO_4)_2$. R_{int}, R_F, R_{F2} and R_{F2w}, the R-factors for conventional Rietveld refinement.

Parameter	Value
Crystal system	Hexagonal
Space group	$P\bar{3}$
Temperature (K)	250
Z	1
a (Å)	5.284(1)
c (Å)	6.980(8)
V (Å^3)	168.801(5)
Extinction coefficient	0.2964
No. reflections; R_{int}	2664; 4.72
No. independent reflections	480
R_{F2}; $R_{F2\omega}$	3.89; 5.10
R_F; χ^2	2.04; 1.12

TABLE II. Atomic positions and parameters of $Na_2BaNi(PO_4)_2$ at 250 K. Occ., occupancy.

Atom	Site	Occ.	x	y	z	U_{eq}
Ba	1a	1	0	0	0	0.0081(2)
Ni	1b	1	0	0	0.5	0.0054(3)
P	2d	1	1/3	2/3	0.24466(13)	0.0054(4)
Na	2d	1	1/3	2/3	0.6782(3)	0.0133(8)
O1	2d	1	1/3	2/3	0.0265(4)	0.0112(12)
O2	6g	1	0.2312(4)	0.8756(4)	0.3212(2)	0.0115(8)

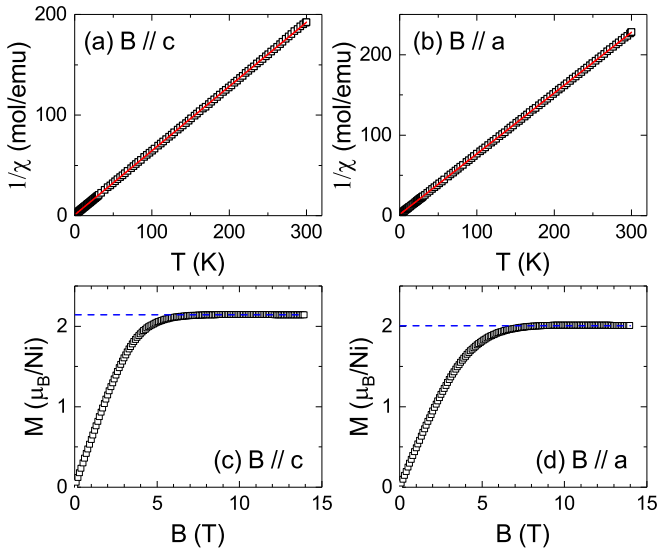

FIG. 2. Temperature dependency of the inverse dc magnetic susceptibility with $B \parallel c$ (a) or $B \parallel a$ (b). The dc magnetization measured at 2 K with $B \parallel c$ (c) or $B \parallel a$ (d). The solid lines in (a) and (b) are linear Curie-Weiss fittings. The dashed lines in (c) and (d) indicate the spin saturation.

C. Specific heat

Figure 5 shows the specific heat C_p measured at zero field. As shown in the inset, the low-temperature data exhibit a broad peak around 600 mK followed by a small but sharp peak at $T_N = 430(3)$ mK. This sharp peak indicates a long-range magnetic ordering, which is consistent with the rapid increase

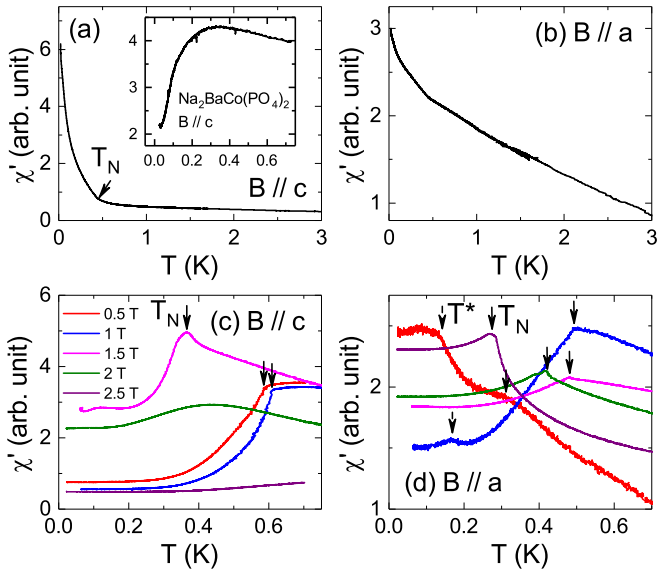

FIG. 3. Temperature dependence of the ac magnetic susceptibility measured at zero dc field but with the ac excitation field along the c axis (a) or a axis (b), or at different dc fields along the c axis (c) or a axis (d). The solid arrows represent T_N, and the dashed arrows represent T^*. For comparison, the inset in (a) shows the ac susceptibility data of the $Na_2BaCo(PO_4)_2$ single crystal with the ac excitation field along the c axis.

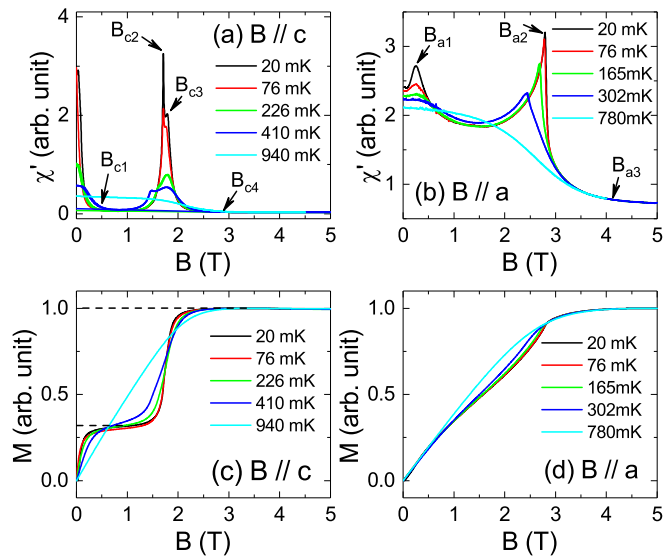

FIG. 4. The dc field dependence of the ac magnetic susceptibility at different temperatures with $B \parallel c$ (a) and $B \parallel a$ (b). Magnetization obtained by integrating the ac susceptibility data for $B \parallel c$ (c) and $B \parallel a$ (d).

at ~400 mK in the zero-field $\chi'(T)$ curve. Apparently, the phonon specific heat is dominant in the high-temperature regime from several tens of kelvins to 300 K. However, it was found that the standard Debye formula cannot fit the high-temperature regime at all. One known reason for the deviations of high-T specific heat from the Debye model is the contribution of optical phonons at high temperatures, which can be described by the Einstein model [56–59]. The phonon spectrum of $Na_2BaNi(PO_4)_2$ should consist of 3 acoustic branches and 39 optical branches. We found that the high-temperature data can be fitted by the formula

$$\begin{aligned} C_{\rm ph} = {} & 3N_D R\left(\frac{T}{\Theta_D}\right)^3 \int_0^{\Theta_D/T} \frac{x^4 e^x}{(e^x-1)^2} dx \\ & + N_{E1} R(\Theta_{E1}/T)^2 \frac{\exp(\Theta_{E1}/T)}{[\exp(\Theta_{E1}/T)-1]^2} \\ & + N_{E2} R(\Theta_{E2}/T)^2 \frac{\exp(\Theta_{E2}/T)}{[\exp(\Theta_{E2}/T)-1]^2} \\ & + N_{E3} R(\Theta_{E3}/T)^2 \frac{\exp(\Theta_{E3}/T)}{[\exp(\Theta_{E2}/T)-1]^2}, \end{aligned} \quad (1)$$

where $x = \hbar\omega/k_B T$, ω is the phonon frequency, k_B is the Boltzmann constant, and R is the universal gas constant. Here, the first term is the contribution of three acoustic phonon branches using the Debye model ($N_D = 3$), while the other terms are the contributions from the optical branches using the Einstein model ($N_{E1} = 12$, $N_{E2} = 15$, and $N_{E3} = 12$). Other parameters are the Debye temperature, $\Theta_D = 165$ K, and three Einstein temperatures, $\Theta_{E1} = 202$ K, $\Theta_{E2} = 451$ K, and $\Theta_{E3} = 1285$ K.

Figures 6(a) and 6(c) show the C_p data measured at $T <$ 4 K and in different fields. With increasing field along the c axis, the peak at T_N first shifts to higher temperatures with abruptly increased intensity while $B < 1$ T, then comes back to lower temperatures with decreased intensity while

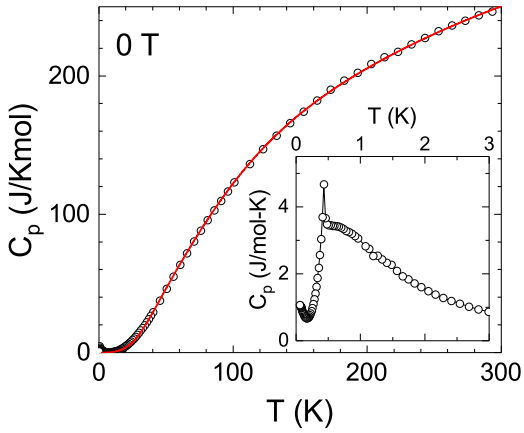

FIG. 5. Temperature dependence of the specific heat measured at zero field. The red line is the fitting of phonon specific heat as described in the main text. The inset highlights the low-temperature specific heat data.

$1 < B < 2$ T, and disappears while $B \geqslant 2$ T. Meanwhile, the broad peak above T_N shifts to higher temperatures around 1–2 K and gains intensity with increasing field. The change in the magnetic entropy below 4 K, ΔS_m, was calculated by integrating $(C_p - C_{ph})/T$ [Fig. 6(b)]. At zero field, the obtained value is 7.46 J/(K mol Ni), which is approaching the expected magnetic entropy value of a spin-1 system, $\Delta S_m = R\ln(2S+1) = R\ln 3$ with $S = 1$. The recovered magnetic entropy below 480 mK (where the sharp peak starts) is 2.83 J/(K mol Ni), which is only 31% of $R\ln 3$. This indicates that a large portion of the magnetic entropy has already

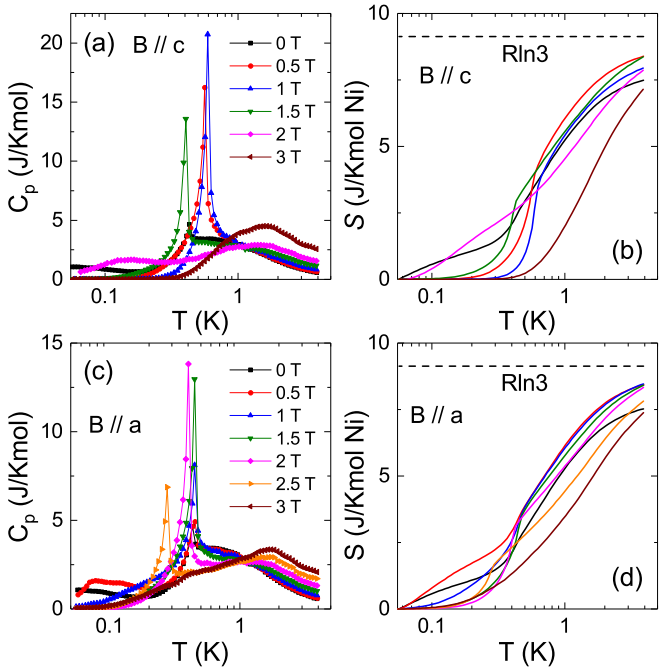

FIG. 6. (a) and (c) Specific heat data with $T < 4$ K and in different magnetic fields along the c axis or the a axis. (b) and (d) The magnetic entropy for $B \parallel c$ and $B \parallel a$, obtained by integrating the magnetic specific heat. The dashed lines show the entropy for $R\ln 3$.

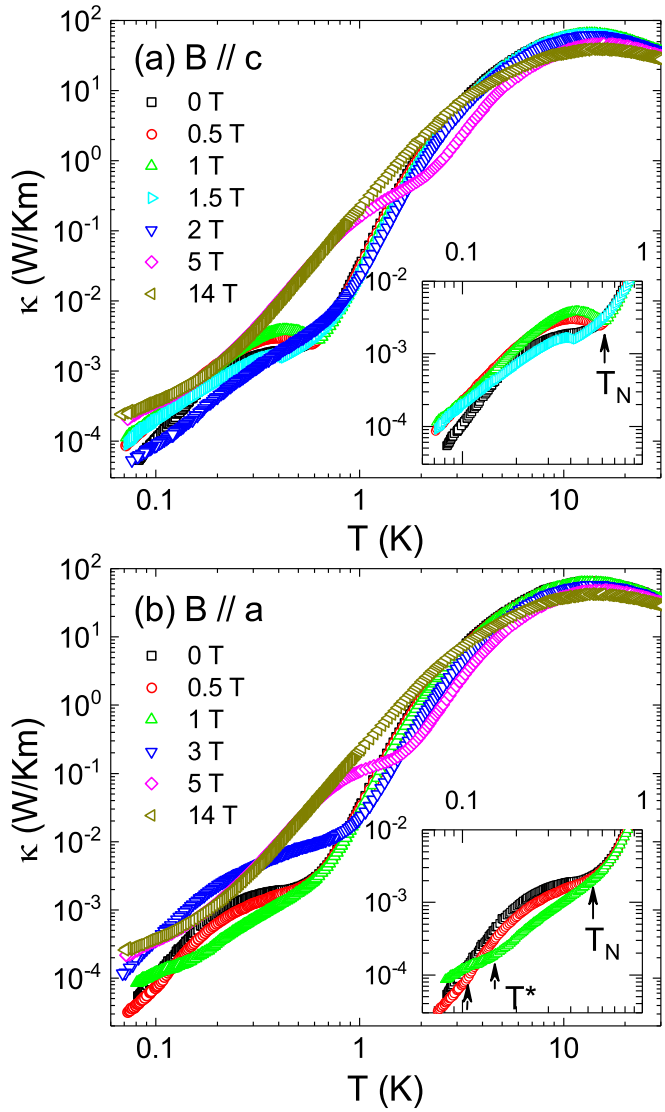

FIG. 7. Temperature dependence of the thermal conductivity measured at different magnetic fields along the c axis (a) or the a axis (b). The insets of (a) and (b) highlight the low-temperature data. The solid arrows represent T_N, and the dashed arrows represent T^*.

been recovered or that there exist strong spin fluctuations above the long-range magnetic ordering temperature T_N. The broad peak around 600 mK at zero field then could be due to the development of short-range correlations. Accordingly, the shift to higher temperatures with increased intensity for this broad peak under fields suggests that the applied field enhances the short-range correlations. Meanwhile, the applied field tunes the long-range ordering in a nonmonotonic way. Similar behaviors were observed for the C_p measured with $B \parallel a$, as shown in Figs. 6(c) and 6(d).

D. Thermal conductivity

Figure 7 shows the temperature dependence of κ measured at different magnetic fields. The zero-field thermal conductivity exhibits a phonon peak at about 14 K with a rather large value of 65 W/Km, which indicates the high crystalline quality of the $Na_2BaNi(PO_4)_2$ sample. In addition, there is

a kinklike feature around 420 mK, which again should be related to the magnetic ordering revealed by both $\chi'(T)$ and C_p. With increasing field along the c axis, as shown in the inset of Fig. 7(a), the kink changes to a dip at 0.5 and 1 T, and the dip position shifts to higher temperatures at 582(5) and 612(5) mK, respectively. With $B = 1.5$ T the dip becomes weaker and shifts to the lower temperature of 429(5) mK, and then it disappears with $B \geqslant 2$ T. This evolution of T_N under fields is similar to that observed from the $\chi'(T)$ and C_p data with $B \parallel c$. With $B = 2$ T and $B = 5$ T, a new kink appears around 640 mK and 1.9 K, respectively. This feature is likely associated with the phonon scattering by spin fluctuations since the C_p data measured at 2 and 3 T indicate that the higher fields enhance the short-range correlations around 1–2 K. With increasing field along the a axis, as shown in Fig. 7(b), the zero-field kink gradually moves to higher temperatures and disappears with $B \geqslant 3$ T, while the 5- and 14-T data are almost the same as those for $B \parallel c$. It is noticed that the 0.5- and 1-T data with $B \parallel a$ show an additional kink around $T^* = 110(2)$ and 160(3) mK, respectively [inset of Fig. 7(b)], which values are consistent with the T^* observed from the $\chi'(T)$ data.

It is well known from many previous studies on the low-dimensional or frustrated spin systems that the anomalies, either the diplike or kinklike features, on the $\kappa(T)$ curves are usually related to the magnetic transitions. In addition, the field dependence of κ can also display similar anomalies at the field-induced magnetic transitions [40,44,55,56,60–62]. Figure 8 shows the $\kappa(B)$ curves at low temperatures for the $Na_2BaNi(PO_4)_2$ single crystal. At 92 mK, the curve with $B \parallel c$ exhibits four minima at B_{c1}, B_{c2}, B_{c3}, and B_{c4}, while there are three minima at B_{a1}, B_{a2}, and B_{a3} for the $B \parallel a$ curve. The values of these critical fields are consistent with those observed from the $\chi'(B)$ data. It is noticed that with increasing temperature, the separation between B_{c2} and B_{c3} increases, which is also observed from the $\chi'(B)$ data. Above certain temperatures, such as 850 mK for $B \parallel c$ and 380 mK for $B \parallel a$, these critical fields are not recognizable.

Another feature of the low-temperature $\kappa(B)$ curves is that the κ at high field is always larger than the zero-field κ and shows saturation behavior. This means that in zero field there is significant magnetic scattering of phonons in a broad temperature region, including both $T < T_N$ and $T > T_N$. In particular, at $T > T_N$ such as 520 and 850 mK, the strong recovery of κ at high field indicates the existence of strong spin fluctuations in zero field that can scatter phonons.

E. Phase diagram

The consistent behaviors for the field dependence of critical temperatures (T_N, T^*) and temperature dependence of all critical fields among the χ', C_p, and κ data strongly suggest the occurrence of field-induced spin state transitions. Accordingly, the magnetic phase diagrams for $B \parallel c$ and $B \parallel a$ were constructed, as shown in Fig. 9. Besides the paramagnetic phase at high temperatures and fully polarized phase at high fields, there are four phases for both cases.

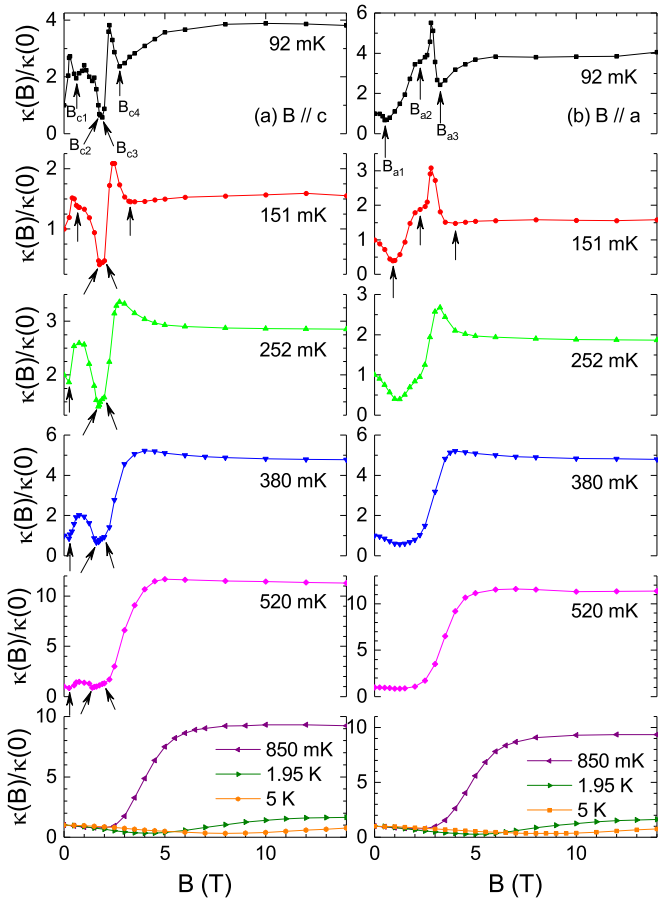

FIG. 8. Thermal conductivity as a function of the magnetic field along the c axis (a) and the a axis (b).

IV. DISCUSSION

Since at low frequency the temperature dependence of the ac $\chi'(T)$ should behave similarly to that of its dc $\chi(T)$, the rapid increase in $\chi'(T)$ below T_N with $B \parallel c$ for $Na_2BaNi(PO_4)_2$ indicates a magnetic ground state with a weak ferromagnetic moment along the c axis. Moreover, the rapid increase in $M(B)$ at low fields [the rapid decrease or, equally, a large peak near 0 T for $\chi'(B)$] also could be seen as a supportive feature for the weak ferromagnetism. This behavior is different from that of several studied ETLAFs. As shown in the inset of Fig. 3(a), the $\chi'(T)$ with $B \parallel c$ for $Na_2BaCo(PO_4)_2$ shows a broad peak at 300 mK followed by a kink at $T_N = 148$ mK [44]. The $\chi(T)$ for the well-studied $Ba_3CoSb_2O_9$ also exhibits a broad peak at 7.0 K followed by an anomaly at $T_N = 3.6$ K [39]. The neutron diffraction data of $Ba_3CoSb_2O_9$ confirmed a 120° spin structure [63]. While such kind of 120° spin structure is common for ETLAFs, it does not lead to a net ferromagnetic moment and therefore should not be the ground state for $Na_2BaNi(PO_4)_2$.

Meanwhile, the reported $Ba_2La_2NiTe_2O_{12}$ exhibits a similar rapid increase in $\chi(T)$ below T_N [47]. Its neutron powder diffraction data confirmed a Y-like triangular spin structure,

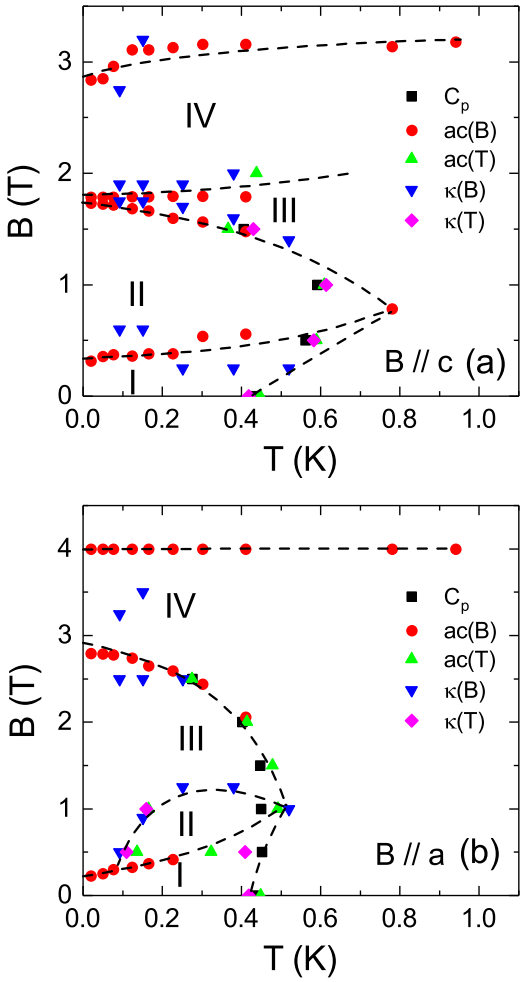

FIG. 9. Magnetic phase diagrams of $Na_2BaNi(PO_4)_2$ for $B \parallel c$ (a) and $B \parallel a$ (b).

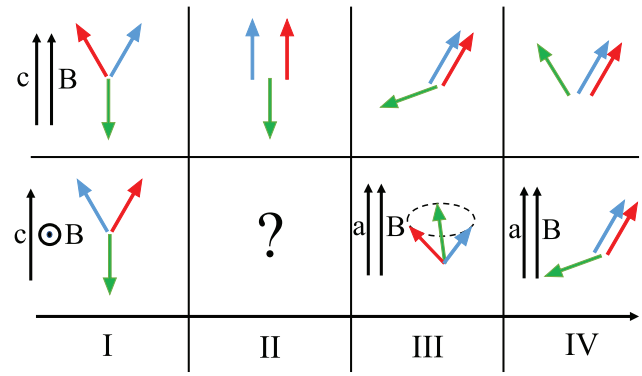

FIG. 10. The proposed spin structure in each phase for $B \parallel c$ (upper row) and $B \parallel a$ (bottom row).

or a canted 120° spin structure, which is in a plane including the crystallographic c axis due to the existence of an easy-axis anisotropy and ferromagnetically stacked along the c axis. In this canted 120° spin structure, the angle θ between the canted sublattice spins and the c axis is smaller than 60°. Accordingly, the sum of the magnetic moments of the three sublattice spins is nonzero but leads to a resultant magnetic moment along the c axis in a triangular layer. Now if the triangular layers are ferromagnetically stacked, all the resultant magnetic moments appearing in the triangular layers will align in the same direction and result in a net magnetic moment along the c axis. Here, we propose that $Na_2BaNi(PO_4)_2$ also has such a magnetic ground state, a canted 120° spin structure ferromagnetically stacked along the c axis with easy-axis anisotropy. Accordingly, we tend to assign phase I for both $B \parallel c$ and $B \parallel a$ to be the canted 120° spin state. While the exact reason for the different magnetic ground states between $Na_2BaNi(PO_4)_2$ and $Na_2BaCo(PO_4)_2$ is not clear, it could be due to the lower symmetry in lattice structure for $Na_2BaNi(PO_4)_2$.

It is obvious that phase II for $B \parallel c$ is the UUD phase because for this phase its magnetization is a 1/3 M_s plateau. Since the UUD phase only survives for $B \parallel c$ in $Na_2BaNi(PO_4)_2$, this again suggests its easy-axis anisotropy as the theory predicted [36]. We can further compare the magnetic phase diagrams of $Na_2BaNi(PO_4)_2$ with those of $Ba_3CoSb_2O_9$. For $Ba_3CoSb_2O_9$ with easy-plane anisotropy, with increasing field along the ab plane, its 120° spin structure at zero field is followed by a canted 120° spin structure, the UUD phase, a coplanar phase (the V phase), and another coplanar phase (the V′ phase) before entering the fully polarized state [40,64–69]. For $B \parallel c$, the 120° spin structure will be followed by an umbrella spin structure and the V phase. Since $Na_2BaNi(PO_4)_2$ has easy-axis anisotropy, we made an analogy between its $B \parallel c$ phase diagram and the $B \parallel a$ phase diagram of $Ba_3CoSb_2O_9$ or its $B \parallel a$ phase diagram and the $B \parallel c$ phase diagram of $Ba_3CoSb_2O_9$. By doing that, we tend to assign phases III and IV with $B \parallel c$ for $Na_2BaNi(PO_4)_2$ to be the V and V′ phases, respectively, and phases III and IV with $B \parallel a$ to be the umbrella and V phases, respectively. Certainly, further studies such as neutron diffraction measurements are needed to verify the spin structures of these phases. Moreover, it is surprising to see a phase II with $B \parallel a$ that is surrounded by phase III. This phase could be a metastable spin state between the canted 120° and the umbrella phase, whose nature again needs future studies to be clarified. The proposed spin structure in each phase is summarized in Fig. 10.

Finally, we want to point out that, to our knowledge, $Na_2BaNi(PO_4)_2$ is a rare example of a spin-1 ETLAF with single-crystalline form that exhibits a series of QSSTs. The other studied spin-1 ETLAFs with Ni^{2+} ions, including $Ba_3NiSb_2O_9$, $Ba_3NiNb_2O_9$, and $Ba_2La_2NiTe_2O_{12}$, are all of polycrystalline form. The availability of single-crystalline $Na_2BaNi(PO_4)_2$ makes it an excellent candidate for future spin-1 ETLAF studies, such as inelastic neutron scattering measurements. For example, for $Ba_3CoSb_2O_9$, unusual spin dynamics have been confirmed by inelastic neutron scattering experiments [39,63,70–73], including strong downward renormalization of the magnon dispersion, rotonlike minima, line broadening throughout the entire Brillouin zone, and intense dispersive excitation continua extending to a high energy that is 6 times the exchange constant. Therefore it will be interesting to see how these features can be affected in a spin-1 ETLAF system, which will provide useful information

to better understand the role of quantum spin fluctuations in ETLAFs.

V. SUMMARY

We have grown single crystals of a spin-1 ETLAF, $Na_2BaNi(PO_4)_2$, and studied its magnetic susceptibility, specific heat, and thermal conductivity at ultralow temperatures. The main experimental results include the following: (i) This material shows a magnetic ordering at 430 mK with a weak ferromagnetic moment along the c axis, (ii) it exhibits a 1/3 magnetization plateau with a magnetic field applied along the c axis, and (iii) there are successive QSSTs for either $B \parallel c$ or $B \parallel a$. It is a rare example of a spin-1 ETLAF with single-crystalline form that exhibits easy-axis spin anisotropy and a series of QSSTs.

ACKNOWLEDGMENTS

This work was supported by the National Natural Science Foundation of China (Grants No. U1832209, No. 11874336, No. 12174361, No. 12104010, and No. 11904003), the Natural Science Foundation of Anhui Province (Grant No. 1908085MA09), and the Innovative Program of Hefei Science Center CAS (Grant No. 2019HSC-CIP001). The work at the University of Tennessee (Q.H., A.B., and H.D.Z.) was supported by the NSF with Grant No. NSF-DMR-2003117. The work performed at NHMFL was supported by Grant No. NSF-DMR-1157490 and the State of Florida. E.X.F. and H.B.C. acknowledge the support of U.S. DOE BES Early Career Award No. KC0402020 under Contract No. DE-AC05-00OR22725.

[1] L. Balents, Nature (London) **464**, 199 (2010).
[2] L. Savary and L. Balents, Rep. Prog. Phys. **80**, 016502 (2016).
[3] Y. Zhou, K. Kanoda, and T.-K. Ng, Rev. Mod. Phys. **89**, 025003 (2017).
[4] J. Knolle and R. Moessner, Annu. Rev. Condens. Matter Phys. **10**, 451 (2019).
[5] C. Nayak, S. H. Simon, A. Stern, M. Freedman, and S. Das Sarma, Rev. Mod. Phys. **80**, 1083 (2008).
[6] T.-H. Han, J. S. Helton, S. Chu, D. G. Nocera, J. A. Rodriguez-Rivera, C. Broholm, and Y. S. Lee, Nature (London) **492**, 406 (2012).
[7] M. Punk, D. Chowdhury, and S. Sachdev, Nat. Phys. **10**, 289 (2014).
[8] M. Kohno, O. A. Starykh, and L. Balents, Nat. Phys. **3**, 790 (2007).
[9] Z. Nussinov, C. D. Batista, B. Normand, and S. A. Trugman, Phys. Rev. B **75**, 094411 (2007).
[10] A. Kitaev and J. Preskill, Phys. Rev. Lett. **96**, 110404 (2006).
[11] M. M. Bordelon, E. Kenney, C. Liu, T. Hogan, L. Posthuma, M. Kavand, Y. Lyu, M. Sherwin, N. P. Butch, C. Brown, M. J. Graf, L. Balents, and S. D. Wilson, Nat. Phys. **15**, 1058 (2019).
[12] J. Ma, J. S. Li, Y. H. Gao, C. L. Liu, Q. Y. Ren, Z. Zhang, Z. Wang, R. Chen, J. Embs, E. X. Feng, F. F. Zhu, Q. Huang, Z. J. Xiang, L. Chen, E. S. Choi, Z. Qu, L. Li, J. F. Wang, H. D. Zhou, Y. X. Su, X. Q. Wang, Q. M. Zhang, and G. Chen, arXiv:2002.09224.
[13] M. Baenitz, Ph. Schlender, J. Sichelschmidt, Y. A. Onykiienko, Z. Zangeneh, K. M. Ranjith, R. Sarkar, L. Hozoi, H. C. Walker, J.-C. Orain, H. Yasuoka, J. van den Brink, H. H. Klauss, D. S. Inosov, and Th. Doert, Phys. Rev. B **98**, 220409(R) (2018).
[14] R. Sarkar, P. Schlender, V. Grinenko, E. Haeussler, P. J. Baker, T. Doert, and H.-H. Klauss, Phys. Rev. B **100**, 241116(R) (2019).
[15] K. M. Ranjith, S. Luther, T. Reimann, B. Schmidt, Ph. Schlender, J. Sichelschmidt, H. Yasuoka, A. M. Strydom, Y. Skourski, J. Wosnitza, H. Kühne, Th. Doert, and M. Baenitz, Phys. Rev. B **100**, 224417 (2019).
[16] Z. Zhang, X. Ma, J. Li, G. Wang, D. T. Adroja, T. P. Perring, W. Liu, F. Jin, J. Ji, Y. Wang, Y. Kamiya, X. Q. Wang, J. Ma, and Q. M. Zhang, Phys. Rev. B **103**, 035144 (2021).
[17] P.-L. Dai, G. Zhang, Y. Xie, C. Duan, Y. Gao, Z. Zhu, E. Feng, Z. Tao, C.-L. Huang, H. Cao, A. Podlesnyak, G. E. Granroth, M. S. Everett, J. C. Neuefeind, D. Voneshen, S. Wang, G. Tan, E. Morosan, X. Wang, H.-Q. Lin, L. Shu, G. Chen, Y. Guo, X. Lu, and P. Dai, Phys. Rev. X **11**, 021044 (2021).
[18] J. Xing, L. D. Sanjeewa, J. Kim, G. R. Stewart, A. Podlesnyak, and A. S. Sefat, Phys. Rev. B **100**, 220407(R) (2019).
[19] T. Xie, J. Xing, S. E. Nikitin, S. Nishimoto, M. Brando, P. Khanenko, J. Sichelschmidt, L. D. Sanjeewa, A. S. Sefat, and A. Podlesnyak, arXiv:2106.12451.
[20] J. A. Paddison, M. Daum, Z. Dun, G. Ehlers, Y. Liu, M. B. Stone, H. Zhou, and M. Mourigal, Nat. Phys. **13**, 117 (2017).
[21] Y. Shen, Y.-D. Li, H. Wo, Y. Li, S. Shen, B. Pan, Q. Wang, H. C. Walker, P. Steffens, M. Boehm, Y. Hao, D. L. Quintero-Castro, L. W. Harriger, M. D. Frontzek, L. Hao, S. Meng, Q. Zhang, G. Chen, and J. Zhao, Nature (London) **540**, 559 (2016).
[22] Y. Li, H. Liao, Z. Zhang, S. Li, F. Jin, L. Ling, L. Zhang, Y. Zou, L. Pi, Z. Yang, J. Wang, Z. Wu, and Q. Zhang, Sci. Rep. **5**, 16419 (2015).
[23] Y. Li, D. Adroja, D. Voneshen, R. I. Bewley, Q. M. Zhang, A. A. Tsirlin, and P. Gegenwart, Nat. Commun. **8**, 15814 (2017).
[24] Y. Shen, Y.-D. Li, H. Walker, P. Steffens, M. Boehm, X. Zhang, S. Shen, H. Wo, G. Chen, and J. Zhao, Nat. Commun. **9**, 4138 (2018).
[25] Y. Li, D. Adroja, P. K. Biswas, P. J. Baker, Q. Zhang, J. Liu, A. A. Tsirlin, P. Gegenwart, and Q. Zhang, Phys. Rev. Lett. **117**, 097201 (2016).
[26] Y.-D. Li, Y.-M. Lu, and G. Chen, Phys. Rev. B **96**, 054445 (2017).
[27] Y.-D. Li and G. Chen, Phys. Rev. B **96**, 075105 (2017).
[28] X. Zhang, F. Mahmood, M. Daum, Z. Dun, J. A. M. Paddison, N. J. Laurita, T. Hong, H. Zhou, N. P. Armitage, and M. Mourigal, Phys. Rev. X **8**, 031001 (2018).
[29] Y. Xu, J. Zhang, Y. S. Li, Y. J. Yu, X. C. Hong, Q. M. Zhang, and S. Y. Li, Phys. Rev. Lett. **117**, 267202 (2016).
[30] Z. Ma, J. Wang, Z. Y. Dong, J. Zhang, S. Li, S. H. Zheng, Y. Yu, W. Wang, L. Che, K. Ran, S. Bao, Z. Cai, P. Cermák, A. Schneidewind, S. Yano, J. S. Gardner, X. Lu, S. L. Yu, J. M. Liu, S. Li *et al.* Phys. Rev. Lett. **120**, 087201 (2018).

[31] Z. Zhu, P. A. Maksimov, S. R. White, and A. L. Chernyshev, Phys. Rev. Lett. **119**, 157201 (2017).

[32] Z. Zhu, P. A. Maksimov, S. R. White, and A. L. Chernyshev, Phys. Rev. Lett. **120**, 207203 (2018).

[33] I. Kimchi, A. Nahum, and T. Senthil, Phys. Rev. X **8**, 031028 (2018).

[34] Q. Luo, S. J. Hu, B. Xi, J. Z. Zhao, and X. Q. Wang, Phys. Rev. B **95**, 165110 (2017).

[35] A. Chubukov and D. Golosov, J. Phys.: Condens. Matter **3**, 69 (1991).

[36] S. Miyashita, J. Phys. Soc. Jpn. **55**, 3605 (1986).

[37] Y. Shirata, H. Tanaka, A. Matsuo, and K. Kindo, Phys. Rev. Lett. **108**, 057205 (2012).

[38] T. Susuki, N. Kurita, T. Tanaka, H. Nojiri, A. Matsuo, K. Kindo, and H. Tanaka, Phys. Rev. Lett. **110**, 267201 (2013).

[39] H. D. Zhou, C. Xu, A. M. Hallas, H. J. Silverstein, C. R. Wiebe, I. Umegaki, J. Q. Yan, T. P. Murphy, J. H. Park, Y. Qiu, J. R. D. Copley, J. S. Gardner, and Y. Takano, Phys. Rev. Lett. **109**, 267206 (2012).

[40] N. A. Fortune, Q. Huang, T. Hong, J. Ma, E. S. Choi, S. T. Hannahs, Z. Y. Zhao, X. F. Sun, Y. Takano, and H. D. Zhou, Phys. Rev. B **103**, 184425 (2021).

[41] M. Lee, J. Hwang, E. S. Choi, J. Ma, C. R. Dela Cruz, M. Zhu, X. Ke, Z. L. Dun, and H. D. Zhou, Phys. Rev. B **89**, 104420 (2014).

[42] K. Yokota, N. Kurita, and H. Tanaka, Phys. Rev. B **90**, 014403 (2014).

[43] Y. Kojima, M. Watanabe, N. Kurita, H. Tanaka, A. Matsuo, K. Kindo, and M. Avdeev, Phys. Rev. B **98**, 174406 (2018).

[44] N. Li, Q. Huang, X. Y. Yue, W. J. Chu, Q. Chen, E. S. Choi, X. Zhao, H. D. Zhou, and X. F. Sun, Nat. Commun. **11**, 4216 (2020).

[45] Y. Shirata, H. Tanaka, T. Ono, A. Matsuo, K. Kindo, and H. Nakano, J. Phys. Soc. Jpn. **80**, 093702 (2011).

[46] J. Hwang, E. S. Choi, F. Ye, C. R. Dela Cruz, Y. Xin, H. D. Zhou, and P. Schlottmann, Phys. Rev. Lett. **109**, 257205 (2012).

[47] M. Saito, M. Watanabe, N. Kurita, A. Matsuo, K. Kindo, M. Avdeev, H. O. Jeschke, and H. Tanaka, Phys. Rev. B **100**, 064417 (2019).

[48] J. G. Cheng, G. Li, L. Balicas, J. S. Zhou, J. B. Goodenough, C. Xu, and H. D. Zhou, Phys. Rev. Lett. **107**, 197204 (2011).

[49] G. Chen, M. Hermele, and L. Radzihovsky, Phys. Rev. Lett. **109**, 016402 (2012).

[50] J. A. Quilliam, F. Bert, A. Manseau, C. Darie, C. Guillot-Deudon, C. Payen, C. Baines, A. Amato, and P. Mendels, Phys. Rev. B **93**, 214432 (2016).

[51] B. Fåk, S. Bieri, E. Canévet, L. Messio, C. Payen, M. Viaud, C. Guillot-Deudon, C. Darie, J. Ollivier, and P. Mendels, Phys. Rev. B **95**, 060402(R) (2017).

[52] R. Zhong, S. Guo, G. Xu, Z. Xu, and R. J. Cava, Proc. Natl. Acad. Sci. USA **116**, 14505 (2019).

[53] J. Rodriguez-Carvajal, Phys. B (Amsterdam) **192**, 55 (1993).

[54] Z. L. Dun, M. Lee, E. S. Choi, A. M. Hallas, C. R. Wiebe, J. S. Gardner, E. Arrighi, R. S. Freitas, A. M. Arevalo-Lopez, J. P. Attfield, H. D. Zhou, and J. G. Cheng, Phys. Rev. B **89**, 064401 (2014).

[55] X. Rao, G. Hussain, Q. Huang, W. J. Chu, N. Li, X. Zhao, Z. Dun, E. S. Choi, T. Asaba, L. Chen, L. Li, X. Y. Yue, N. N. Wang, J.-G. Cheng, Y. H. Gao, Y. Shen, J. Zhao, G. Chen, H. D. Zhou, and X. F. Sun, Nat. Commun. **12**, 4949 (2021).

[56] J. D. Song, X. M. Wang, Z. Y. Zhao, J. C. Wu, J. Y. Zhao, X. G. Liu, X. Zhao, and X. F. Sun, Phys. Rev. B **95**, 224419 (2017).

[57] P. Svoboda, P. Javorský, M. Diviš, V. Sechovský, F. Honda, G. Oomi, and A. A. Menovsky, Phys. Rev. B **63**, 212408 (2001).

[58] J. Hemberger, M. Hoinkis, M. Klemm, M. Sing, R. Claessen, S. Horn, and A. Loidl, Phys. Rev. B **72**, 012420 (2005).

[59] P. Janíček, Č. Drašar, P. Lošt'ák, J. Vejpravová, and V. Sechovský, Phys. B (Amsterdam) **403**, 3553 (2008).

[60] I. A. Leahy, C. A. Pocs, P. E. Siegfried, D. Graf, S.-H. Do, K.-Y. Choi, B. Normand, and M. Lee, Phys. Rev. Lett. **118**, 187203 (2017).

[61] R. Hentrich, A. U. B. Wolter, X. Zotos, W. Brenig, D. Nowak, A. Isaeva, T. Doert, A. Banerjee, P. Lampen-Kelley, D. G. Mandrus, S. E. Nagler, J. Sears, Y.-J. Kim, B. Büchner, and C. Hess, Phys. Rev. Lett. **120**, 117204 (2018).

[62] J. A. H. M. Buys and W. J. M. de Jonge, Phys. Rev. B **25**, 1322 (1982).

[63] J. Ma, Y. Kamiya, T. Hong, H. B. Cao, G. Ehlers, W. Tian, C. D. Batista, Z. L. Dun, H. D. Zhou, and M. Matsuda, Phys. Rev. Lett. **116**, 087201 (2016).

[64] D. Yamamoto, G. Marmorini, and I. Danshita, Phys. Rev. Lett. **112**, 127203 (2014).

[65] G. Marmorini, D. Yamamoto, and I. Danshita, Phys. Rev. B **93**, 224402 (2016).

[66] D. Sellmann, X.-F. Zhang, and S. Eggert, Phys. Rev. B **91**, 081104(R) (2015).

[67] G. Koutroulakis, T. Zhou, Y. Kamiya, J. D. Thompson, H. D. Zhou, C. D. Batista, and S. E. Brown, Phys. Rev. B **91**, 024410 (2015).

[68] A. Sera, Y. Kousaka, J. Akimitsu, M. Sera, T. Kawamata, Y. Koike, and K. Inoue, Phys. Rev. B **94**, 214408 (2016).

[69] X. Z. Liu, O. Prokhnenko, D. Yamamoto, M. Bartkowiak, N. Kurita, and H. Tanaka, Phys. Rev. B **100**, 094436 (2019).

[70] S. Ito, N. Kurita, H. Tanaka, S. Ohira-Kawamura, K. Nakajima, S. Itoh, K. Kuwahara, and K. Kakurai, Nat. Commun. **8**, 235 (2017).

[71] Y. Kamiya, L. Ge, T. Hong, Y. Qiu, D. L. Quintero-Castro, Z. Lu, H. B. Cao, M. Matsuda, E. S. Choi, C. D. Batista, M. Mourigal, H. D. Zhou, and J. Ma, Nat. Commun. **9**, 2666 (2018).

[72] D. Macdougal, S. Williams, D. Prabhakaran, R. I. Bewley, D. J. Voneshen, and R. Coldea, Phys. Rev. B **102**, 064421 (2020).

[73] R. Verresen, R. Moessner, and F. Pollmann, Nat. Phys. **15**, 750 (2019).